ELSEVIER

Contents lists available at ScienceDirect

### Earth and Planetary Science Letters

www.elsevier.com/locate/epsl



## The evolution of lithium isotope signatures in fluids draining actively weathering hillslopes



Jon K. Golla <sup>a,\*</sup>, Marie L. Kuessner <sup>b,c</sup>, Michael J. Henehan <sup>c</sup>, Julien Bouchez <sup>b</sup>, Daniella M. Rempe <sup>d</sup>, Jennifer L. Druhan <sup>a,b</sup>

- <sup>a</sup> Department of Geology, University of Illinois at Urbana-Champaign, Urbana, IL 61801, USA
- <sup>b</sup> Institut de Physique du Globe de Paris, Sorbonne Paris Cité, Université Paris Diderot, CNRS, 75238 Paris, France
- <sup>c</sup> Section 3.3 Earth Surface Geochemistry, GFZ German Research Centre for Geosciences, Telegrafenberg, 14473 Potsdam, Germany
- <sup>d</sup> Jackson School of Geosciences, University of Texas at Austin, Austin, TX 78712, USA

#### ARTICLE INFO

# Article history: Received 25 October 2020 Received in revised form 29 March 2021 Accepted 4 May 2021 Available online xxxx Editor: L. Derry

Keywords: lithium isotopes silicate weathering reactive transport Critical Zone

#### ABSTRACT

The stable isotopes of lithium (Li) serve as a robust proxy of silicate weathering. The fate and transport of these isotopes in the dissolved load of major rivers have been characterized to infer changes in both contemporary weathering regimes and paleo-conditions. In this contribution, we deconvolve this integrated signal into the individual processes that fractionate Li at the inception of silicate weathering by directly measuring Li isotope ratios of waters ( $\delta^7$ Li) transiting through a rapidly eroding first-order hillslope. We use these data to develop a multicomponent reactive transport framework, which shows that net dissolution of weathered material generates light  $\delta^7 {
m Li}$  signatures (as low as -9.2%) in the shallow portion of the vadose zone. An increase in  $\delta^7 \text{Li}$  deeper into the vadose zone (as much as +18%) reflects an increasing contribution of secondary mineral formation. Below the water table, congruent weathering occurs and imparts elevated cation concentrations and bedrock  $\delta^7$ Li. Silicate weathering continues within the saturated zone as groundwater travels downslope ( $\delta^7 \text{Li} = +13 \text{ to } + 24\%$ ) to the stream. The stream signatures ( $\delta^7 \text{Li} = +28 \text{ to } +29\%$ ) reflect the terminus of this network of silicate weathering reactions and the relative magnitude of each contributing process (e.g., transitions in secondary mineral formation, dissolution of weathered material). We show that fluid progressing through the weathering profile of this first-order hillslope is distinguished by a sequence of characteristic Li isotope signatures, which can be reproduced in a forward, process-based model framework. This model development offers an improved quantitative basis for the use of metal(loid) stable isotopes in disentangling catchment-scale chemical weathering fluxes.

© 2021 The Author(s). Published by Elsevier B.V. This is an open access article under the CC BY-NC-ND license (http://creativecommons.org/licenses/by-nc-nd/4.0/).

#### 1. Introduction

Landscape denudation occurs as a result of physiochemical breakdown of rock within the weathering profile and removal via either solute export or mechanical erosion (Ahnert, 1970; Garrels and Mackenzie, 1971; Raymo et al., 1988; Riebe et al., 2001). In environments where fresh bedrock is shallow and accessed by meteoric fluids, the chemical weathering component of denudation releases geogenic nutrients vital to ecosystem function, generates the mineral building blocks of soil, and sets the chemical composition of headwaters (Anderson et al., 2007; Bormann and Likens, 1967; Stallard and Edmond, 1983).

Indirect inference from weathered bedrock elemental composition (e.g., Brantley and Lebedeva, 2011; Brimhall and Dietrich, 1987) and relatively large solute concentration gradients in soil water (e.g., Anderson et al., 2002; White et al., 2009) suggest high silicate weathering rates in the vadose zone of upland hillslopes. However, direct observations of weathering in the vadose zone are scarce, primarily due to the difficulty of accessing fluids in the region below maximum trench or auger depth and above the shallowest levels sampled by groundwater wells. Thus, the water-rock interactions of the vadose zone are largely appraised from integrated samples such as the underlying groundwater or solid-phase cores. Another approach has been to infer weathering pathways from samples collected much further along catchment flow paths, such as in the streams and rivers that drain from the Critical Zone (e.g., Calmels et al., 2011; Torres et al., 2015; Gaillardet et al., 1999). While multiple biogeochemical catchment processes constitute this riverine signature, the extent to which the reactive

<sup>\*</sup> Corresponding author.

E-mail address: jgolla2@illinois.edu (J.K. Golla).

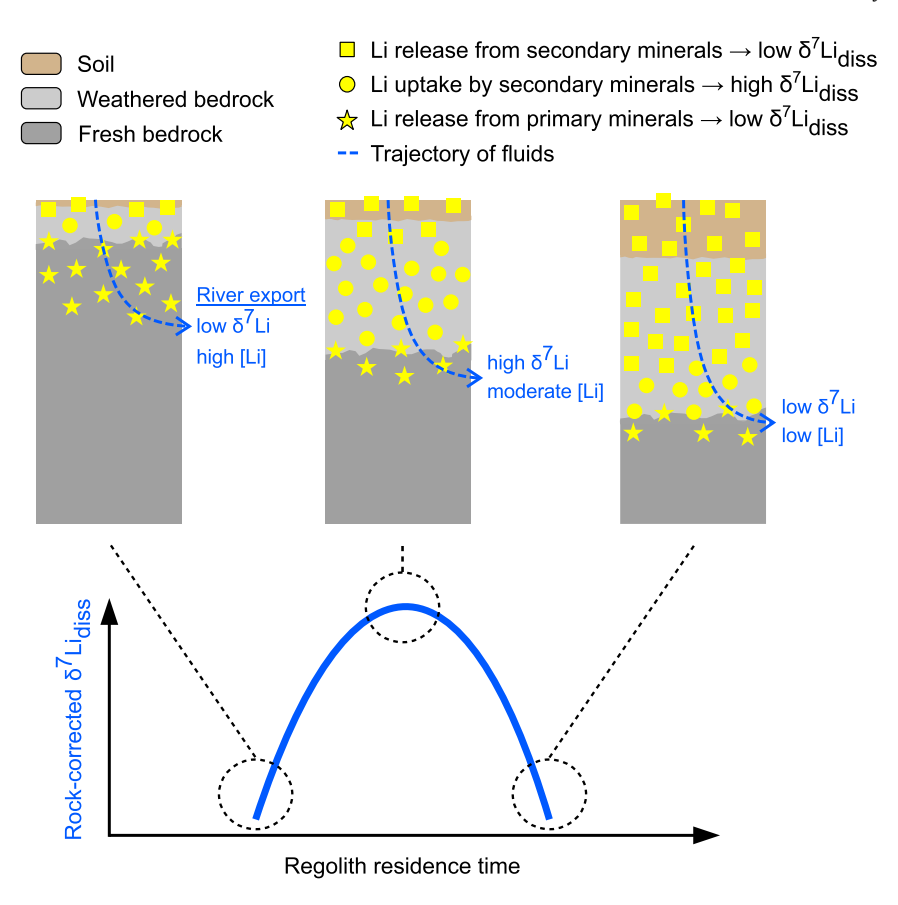


**Fig. 1.** A conceptual diagram linking regolith residence time to dissolved  $\delta^7 \text{Li}$  signatures ( $\delta^7 \text{Li}_{\text{diss}}$ ) (Bouchez et al., 2013). This relationship has been supported by large river studies (e.g., Dellinger et al., 2015; Wang et al., 2015).  $\delta^7 \text{Li}_{\text{diss}}$  resembling rock-like values are observed when dissolution of fresh bedrock (infiltration through thin regolith in settings where erosion occurs more quickly than weathering) or secondary clays (infiltration through thick regolith; typical of settings where erosion occurs more slowly than weathering) is dominant. Peak  $\delta^7 \text{Li}_{\text{diss}}$  values are obtained when secondary mineral formation is dominant (infiltration through moderately thick regolith; typical of settings where erosion and weathering rates are equal or similar). (For interpretation of the colors in the figure(s), the reader is referred to the web version of this article.)

pathways of weathering that actively drive regolith development (i.e. weathered bedrock and soil) are reflected remains unclear.

Lithium (Li) is an established and effective tracer of silicate weathering. The partitioning of its stable isotopes (<sup>6</sup>Li and <sup>7</sup>Li) reflects the preferential incorporation of <sup>6</sup>Li into the secondary mineral byproducts (i.e., clays and oxides) of silicate weathering (Huh et al., 2001; Kısakürek et al., 2004, 2005; Pistiner and Henderson, 2003; Rudnick et al., 2004; Tomascak, 2004). Li is mostly contained in silicate rocks (Kısakürek et al., 2005; Millot et al., 2010) and its isotopes are unaffected by biological uptake (Lemarchand et al., 2010; Pogge von Strandmann et al., 2016), making this tool widely applicable to parsing weathering signatures in the Critical Zone.

From this basis, riverine Li isotope signatures are increasingly being interpreted as a result of regolith residence time (Fig. 1; Bouchez et al., 2013). This model conceptualizes  $\delta^7 \text{Li}$  signals as an integration of three key processes (and associated fractionation factors,  $\alpha_{\text{solid-diss}}$ ): (1) Li release to solution from primary minerals ( $\alpha \approx 1.0$ ); (2) formation of Li-bearing secondary phases ( $\alpha < 1.0$ ); (3) Li release to solution from Li-bearing soil secondary phases during re-equilibration and evolution to Li-poorer phases ( $\alpha \approx 1.0$ ). The result is a relationship between riverine  $\delta^7 \text{Li}$  signatures and the intensity of chemical weathering of a given landscape.

Although this framework is supported by empirical evidence of riverine isotope signatures (e.g., Dellinger et al., 2015; Henchiri et al., 2016; Huh et al., 2001; Misra and Froelich, 2012; Pogge von Strandmann et al., 2014; Wang et al., 2015), the validity of the underlying mechanisms has yet to be demonstrated within the fluids draining an active weathering profile. This study will investigate whether the isotope signatures of fluid vertically draining through

the interior of hillslopes are described by the same sequence of processes and how this signal propagates further into the fluvial drainage networks of watersheds. Within the Bouchez et al. (2013) framework, process (3) would prevail in the upper soil horizons where clays formed at depth re-equilibrate with infiltrating dilute waters, sometimes rich in dissolved organic carbon that aid solubilization of major silicate- and oxide-forming metals such as Al or Fe. Process (2) would be most prominent deeper in the regolith where percolating waters are solute-laden enabling the formation of cation-rich clays. Process (1) would dominate where fluids are in contact with fresh bedrock. Hence, in a weathering profile we would anticipate that (Fig. 2):

- 1. The fluid composition both at the top and base of the profile would inherit the isotopic signature of the dissolving clays and bedrock, respectively (Burton and Vigier, 2012; Pistiner and Henderson, 2003; Wimpenny et al., 2010). At intermediate depth, dissolved  $^6$ Li would become depleted (i.e., fluid will have higher  $\delta^7$ Li) in the zone where secondary minerals are actively precipitating.
- 2. The  $\delta^7 \text{Li}$  of the new clays formed from this fluid would essentially track the fluid  $\delta^7 \text{Li}$  value with depth and be offset by the fractionation factor associated with mineral formation and/or adsorption reactions.
- 3. The bulk regolith  $\delta^7 \text{Li}$  composition can shift relative to the bedrock. The specific  $\delta^7 \text{Li}$  value of this bulk solid is a function of the length scale over which regolith is produced and the relative contribution of newly forming Li-bearing secondary

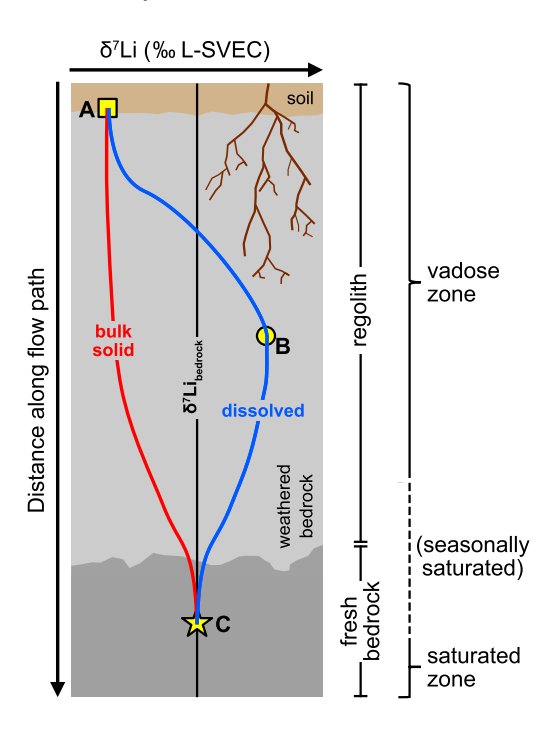


**Fig. 2.** A conceptual interpretation of dissolved and solid-phase lithium isotope compositions in a weathering profile. The lettered markers denote key stages of the hypothesized evolution of the dissolved profile. Dissolution conditions dominate during infiltration in the near-surface (A) and reaction with fresh bedrock at depth (C) results in an inheritance of the solid-phase isotopic composition. The bulk solid-phase isotope composition depends on the balance between new clays and secondary minerals originally in the bedrock. Although a newly formed clay could be relatively isotopically heavy (especially if precipitated from  $^6$ Li-depleted fluids), we reflect conditions in which the overall isotopic composition of clays in the weathering profile is generally lighter than that of the fresh bedrock (e.g., Rudnick et al., 2004; Steinhoefel et al., 2021; Zhang et al., 2021a). Therefore, in the case of (A), a low dissolved  $δ^7$ Li value can be generated by preferential dissolution of  $^6$ Li-enriched weathering byproducts (Lemarchand et al., 2010; Pistiner and Henderson, 2003). In between these points, secondary mineral formation predominates deeper into the regolith (B) and imparts high  $δ^7$ Li values to the fluid.

minerals (point 2 above) versus those originally present in the bedrock and retained across the weathering profile.

Here, we report the first direct measurements of the Li isotope ratios of fluids draining an actively weathering vadose zone. We combine these observations with samples of groundwater laterally transiting the hillslope and the stream that drains the base of the hillslope. These data are used to validate a forward, process-based reactive transport framework capable of quantifying the contributions of multiple silicate weathering reactions operating in tandem through the open, through-flowing structure of this hillslope. With this data-validated, isotope-enabled model framework, we offer the first direct analysis of the inception of silicate weathering signatures generated via infiltration of fluids through unsaturated regolith and how these signals are further affected by transport through the saturated zone to the river network.

#### 2. Study area

We leverage an extensively-instrumented, small, and steep  $(4,000 \text{ m}^2 \text{ and } \sim 32^\circ; \text{ Kim et al., 2014; Salve et al., 2012) hillslope, named "Rivendell", in the Eel River Critical Zone Observatory (ER-CZO) (Fig. 3). Rivendell sits within the Angelo Coast Range Reserve and is located within the 14-km² Elder Creek watershed, which is a tributary of the South Fork Eel River in northern California. The climate of the region is Mediterranean typified by arid summers and wet winters. Most precipitation occurs as rain within a 5-6 month period, with a mean annual rate of 1,900 mm/yr (Salve$ 

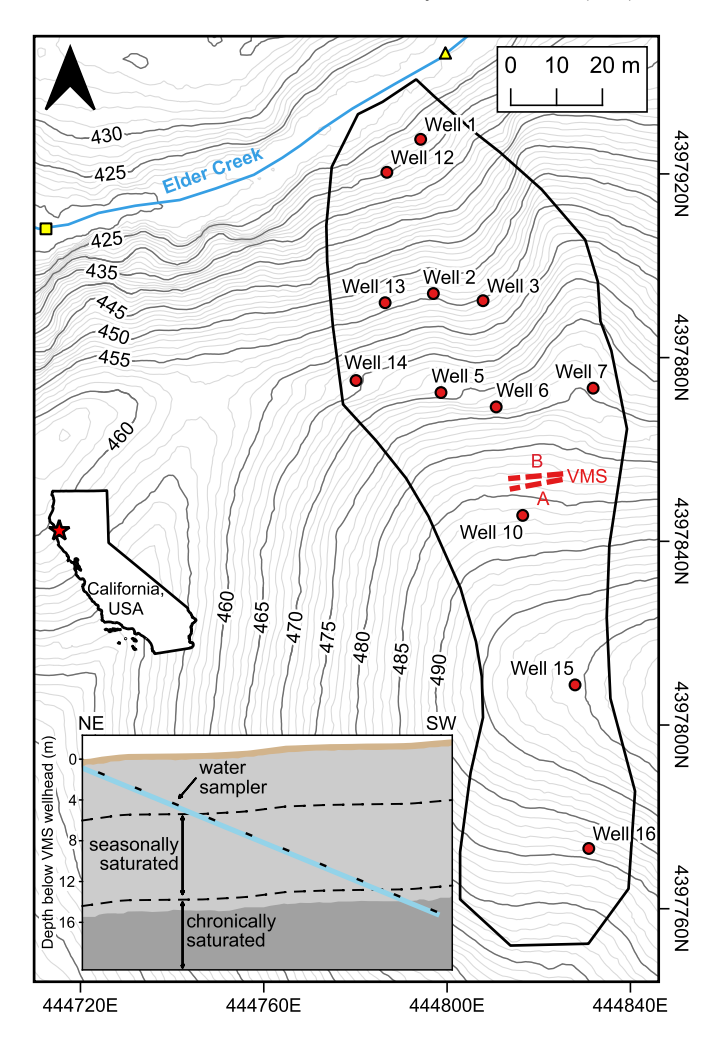


**Fig. 3.** Site map of the ERCZO Rivendell hillslope in Mendocino County, California showing the distribution of groundwater wells (red circles) and the Vadose Zone Monitoring System (VMS) apparatus (red dashed lines), which consists of two subvertical sleeves (VMS-A and VMS-B). The approximate locations of the Elder Creek water sample (yellow square) and a U.S. Geological Survey stream gage (#11475560; yellow triangle) are also shown. The black outline marks the Rivendell watershed boundary. Elevation data are derived from a National Center for Airborne Laser Mapping survey in 2014. Contours shown are for 1-m intervals, which are labeled every 5 m. The inset figure is a cross-section schematic of VMS-A showing the orientation of the instrumentation. The color scheme for respective subsurface layers is similar to that used in Figs. 1 and 2 (brown = soil; light gray = weathered bedrock).

et al., 2012). The hillslope is covered by a dense, mature conifer forest with sparse undergrowth. Rivendell affords an ideal setting for examining silicate weathering dynamics between the soil and stream, given the thick actively weathering bedrock (4-25 m) relative to thin soil (0.5-0.75 m) (Kim et al., 2014, 2017).

Rivendell is underlain by turbidite sequences consisting of argillaceous shale interbedded with some minor beds of arkosic graywacke and conglomerate. The bedrock is mapped as Eocene Yager terrane of the Coastal Belt of the Franciscan Complex, which has experienced low-grade metamorphism (McLaughlin et al., 2000). The mineralogy of this parent material is a combination of primary minerals and pre-existing secondary phases: quartz (24.8%), albite (21.9%), chlorite (18.3%), smectite (12.6%), illite (7.4%), kaolinite (3.5%), and carbonates (2.2%) (Gu et al., 2020). Contemporary erosion rates are approximately 0.2-0.4 mm/yr (Fuller et al., 2009).

Recent sampling and instrumentation advancements at the ERCZO have allowed direct access to waters hosted within the bedrock vadose zone. Monitoring to date indicates that roots ac-

tively circulate water within the bedrock underlying soils (Rempe and Dietrich, 2018) and sustain enhanced reactivity (Tune et al., 2020; Rempe and Dietrich, 2018), which leads to high silicate weathering rates that are dependent on the evolving composition of the uplifting solid and infiltrating fluid (Druhan et al., 2017; Wang, 2019).

#### 3. Methods

#### 3.1. Water sampling

Water samples were collected from a network of groundwater wells and Elder Creek (Fig. 3) between January 5 and January 8 in 2017. Fluids transiting the vadose zone were obtained from a unique Vadose Zone Monitoring System (VMS) on March 3, 2019. The VMS consists of discrete water samplers distributed throughout the weathering profile (Fig. 3). The subvertical orientation of the VMS allows for synoptic collection of fluids at different depths. More details about its functioning are described in Dahan et al. (2009) and Turkeltaub et al. (2015). At Rivendell, there are two parallel units, VMS-A and VMS-B, which altogether host 20 sampling ports. Port depths are reported in Table 1. The deepest five ports were below the water table (i.e., in the saturated zone) at the time of sampling and thus collecting shallow groundwater. Unlike the discrete VMS ports, the wells are continuously slotted throughout their depth and therefore represent a mixture of groundwaters. All water samples intended for cation and Li isotope analysis were filtered at 0.22 µm (to retain only the dissolved load) into pre-washed polyethylene bottles, acidified with tripledistilled, concentrated HNO<sub>3</sub> to a target pH of <2, and refrigerated at  $4^{\circ}$ C.

#### 3.2. Analytical procedure

Analytical work was done at the HELGES laboratory of GFZ Helmholtz Centre Potsdam (GFZ) and the PARI analytical platform of the Institut de physique du globe de Paris (IPGP). Water samples and a bedrock solid-phase sample were processed prior to isotopic analysis via the chemical purification scheme developed by James and Palmer (2000) and modified by Zhang et al. (2021b). Aliquots of digested samples were loaded onto a column packed with 2 mL of Bio Rad AG50-X12 cation-exchange resin. Li was separated from the sample matrix via elution in 0.2-M HCl. Li isotope measurements were made using a Thermo Scientific Neptune MC-ICP-MS at GFZ. Processed and re-dried samples were dissolved in 0.5-N HNO<sub>3</sub> to make up a 20 ng/mL Li solution and introduced into the plasma through an APEX-HydroFluoric (Elemental Scientific) desolvating nebulizer. The instrument was operated under conditions similar to those outlined in Millot et al. (2004). The instrument was tuned to achieve a stable <sup>7</sup>Li/<sup>6</sup>Li ratio (standard deviation of  $<10^{-3}$  over 12 cycles) and a low blank-to-sample ratio for the  $^{7}$ Li signal (<0.8%). Analyses were done using standard-sample bracketing as:

$$\delta^{7} \text{Li}(\%) = \left(\frac{\frac{^{7}\text{Li}}{^{6}\text{Li}} \frac{}{\text{sample}}}{\frac{^{7}\text{Li}}{^{6}\text{Li}} \frac{}{\text{L-SVEC}}} - 1\right) \times 1000, \tag{1}$$

where the L-SVEC Li carbonate reference material (Flesch et al., 1973) is the bracketing standard. Full external reproducibility (incorporating uncertainty from sample preparation, column chemistry, and analysis) was approximated by analysis of reference materials with each sample set, with a similar mass of Li ( $\sim$ 50 ng) used for samples and reference materials. Uncertainty applied to sample measurements is based on the repeat measurement of OSIL

Atlantic seawater ( $\delta^7 \text{Li} = 30.88 \pm 0.76\%$ ); n = 4). Accuracy of Li isotope analysis in other sample matrices was verified by measurements of the reference materials BHVO-2 and IB-2 (basalts) and Till-1 (soil). Values of 4.77  $\pm$  0.09\% (BHVO-2), 4.99  $\pm$  0.06\% (JB-2) are in good agreement with published literature values (Li et al., 2018, and references therein), although we note our value of 7.21  $\pm$  0.27% for Till-1 is somewhat higher than the only published measurement of this material to date (6.4  $\pm$  0.1%; Weynell et al., 2017). Concentrations of major ions and trace elements for well and Elder Creek waters and the digested bedrock sample were analyzed by a high-pressure ion chromatograph (Dionex ICS-300 and -120 for cations and anions, respectively) and an Agilent 7900 quadrupole ICP-MS at IPGP, respectively. VMS cation concentrations were determined at GFZ with a Thermo Scientific iCAP Q ICP-MS. The analytical uncertainties for major (<2%) and trace (<4%) elements were assessed with replicate analyses of the reference material SLRS-5.

#### 3.3. Reactive transport simulations

We employ an isotope-enabled, multicomponent reactive transport model using the open-source CrunchFlow/CrunchTope software (Druhan et al., 2013; Steefel et al., 2015) to simulate the reactive flow of infiltrating precipitation ( $\delta^7 \text{Li} = +31\%$ ; Supplementary Text S1.1) through present-day bulk regolith composing the Rivendell hillslope ( $\delta^7 \text{Li} = -0.57\%$ ); Table 1). Here, we integrate Li and its isotopes into a previously established reactive transport model for the Rivendell vadose zone, which focused on cation solute profiles and solid-phase mineralogy (Wang, 2019). Parameterization of hydraulic properties and initial geochemical conditions are detailed in this prior work. Notably, the present simulations focus on the evolution of the dissolved phase over a relatively short timespan ( $\sim$ 5 pore volumes or 6 yr; Supplementary Text S1.1) and thus erosion and uplift of the solid phase are considered negligible. The model in Wang (2019) is limited to the vadose zone. Thus, we extend the simulation into the saturated zone as a 0-D batchreactor framework that advances through time (a proxy for lateral downslope transport) under fully water-saturated conditions (Supplementary Text S1.2).

Of the pre-existing minerals found in the shale protolith, we selected three clays (smectite, illite and kaolinite) to contain Li as trace substitutions in their stoichiometry (Supplementary Text S1.3). The additional presence of Li in chlorite in the unweathered bedrock (Gu et al., 2020) is explored further in subsection 5.2. To simulate isotopic fractionation, we parse total Li into two components, <sup>7</sup>Li and <sup>6</sup>Li (Table 2). The isotope composition of these clays is initially specified to match the bulk bedrock composition ( $\delta^7 \text{Li} =$ -0.57%; Table 1), while newly precipitating clays are allowed to fractionate through a solid solution with endmembers containing either <sup>7</sup>Li or <sup>6</sup>Li (Druhan et al., 2013). We use an updated version of CrunchFlow/CrunchTope so that dissolution of a mineral configured as a solid solution does not spuriously fractionate Li and instead results in inheritance of the isotopic composition of the dissolving mineral(s) by the reacting water (Burton and Vigier, 2012; Pistiner and Henderson, 2003; Wimpenny et al., 2010). A kinetic fractionation factor is implemented as the difference in kinetic rate constants (i.e.,  $\alpha = {}^{7}k/{}^{6}k$ ) during precipitation of kaolinite and illite. The fractionation factor used for kaolinite formation,  $\alpha_{\text{kaolinite-diss}} = 0.992$ , is based on an earlier study reporting batch experiments under ambient conditions (Li and Liu, 2020). The fractionation factor for illite formation,  $\alpha_{illite-diss} = 0.976$ , is based on an extrapolation of a value determined from a high-temperature illitization experiment to 25 °C (Williams and Hervig, 2005). Importantly, both of these fractionation factors are literature-derived and are not free parameters in these simulations. The rationale for these fractionation factors and the reactive pathways that they rep-

Table 1
Dissolved element concentrations and isotopic compositions for Rivendell waters and digested bedrock sample. Fluid volumes collected from the VMS are limited, so the entirety of the samples collected on 03/03/2019 were devoted to lithium isotope analysis. All concentrations are in μmol/L, except for those of the digested bedrock sample (mmol/kg). Uncertainties for dissolved  $\delta^7$ Li measurements and elemental concentrations are  $\pm 0.76\%$  and typically <5%, respectively. The accuracy of the Li isotope analysis of the bedrock samples is discussed in subsection 3.2.

Sample ID	Location <sup>a</sup>	Sample type	Sampling date	δ <sup>7</sup> Li (‰)	Li	Na	Cl	K	Ca	Mg	SiO <sub>2</sub>	Al
B1	VMS-B (1.1 m)	Vadose zone	3/3/2019	-	0.14	57						
A1	VMS-A (1.7 m)	Vadose zone	3/3/2019	_	0.14	62	_	_	_	_	_	_
B2	VMS-B (2.6 m)	Vadose zone	3/3/2019	_	0.34	45	_	_	_	_	_	_
A2	VMS-A (3.2 m)	Vadose zone	3/3/2019	_	0.17	82	_	_	_	_	_	_
B3	, ,			- -9.24	0.40	56	_	_	_	-	_	-
	VMS-B (4.0 m)	Vadose zone	3/3/2019	-9.24 -3.79	0.51	36 113		-		-		-
A3	VMS-A (4.7 m)	Vadose zone	3/3/2019			94	-	-	-	_	-	-
B4	VMS-B (5.6 m)	Vadose zone	3/3/2019	- 7.64	0.47		-	-	-	_	-	_
A4	VMS-A (6.2 m)	Vadose zone	3/3/2019	-7.64	0.43	109	-	_	-	_	-	-
B5	VMS-B (7.1 m)	Vadose zone	3/3/2019	2.76	0.46	78	-	-	-	-	-	-
B6	VMS-B (8.6 m)	Vadose zone	3/3/2019	4.39	0.59	88	-	-	-	-	-	-
A6	VMS-A (9.2 m)	Vadose zone	3/3/2019	5.96	0.83	171	-	-	-	-	-	-
B7	VMS-B (10.1 m)	Vadose zone	3/3/2019	4.94	0.99	186	-	-	-	-	-	-
A7	VMS-A (10.7 m)	Vadose zone	3/3/2019	9.60	0.67	172	-	-	-	-	-	-
B8	VMS-B (11.6 m)	Vadose zone	3/3/2019	4.20	0.62	97	-	-	-	-	-	-
A8	VMS-A (12.2 m)	Saturated zone	3/3/2019	8.92	0.65	134	-	-	-	-	-	-
B9	VMS-B (13.1 m)	Saturated zone	3/3/2019	14.86	1.20	161	-	-	-	-	-	-
A9	VMS-A (13.7 m)	Saturated zone	3/3/2019	10.46	2.73	148	-	-	-	-	-	-
B10	VMS-B (14.6 m)	Saturated zone	3/3/2019	-	0.53	197	-	-	-	-	-	-
A10	VMS-A (15.2 m)	Saturated zone	3/3/2019	17.28	2.79	888	-	-	-	-	-	-
R-1	Well 2 (420 m)	Saturated zone	1/05/2017	24.56	0.63	261	58	-	-	335	466	0.08
R-3	Well 3	Saturated zone	1/06/2017	-	0.50	215	83	-	-	113	479	0.09
R-4	Well 5 (449 m)	Saturated zone	1/06/2017	-	0.83	348	100	-	-	357	435	0.06
R-6	Well 6 (452 m)	Saturated zone	1/05/2017	-	0.73	246	101	-	-	117	568	0.17
R-7	Well 7 (454 m)	Saturated zone	1/06/2017	12.81	0.45	220	135	-	-	72	582	0.37
R-8	Well 7 (454 m)	Saturated zone	1/06/2017	-	0.46	-	133	-	-	71	580	0.35
R-9	Well 7 (454 m)	Saturated zone	1/06/2017	-	0.47	-	132	-	-	70	568	0.36
R-11	Well 10	Saturated zone	1/06/2017	15.66	0.58	231	92	-	-	79	574	0.16
R-13	Well 12 (402 m)	Saturated zone	1/05/2017	23.74	0.58	363	70	-	-	469	375	0.07
R-15	Well 13 (420 m)	Saturated zone	1/05/2017	-	0.40	274	87	-	-	524	267	0.05
R-17	Well 14 (445 m)	Saturated zone	1/05/2017	-	0.43	196	64	-	-	112	439	0.08
R-18	Well 14 (445 m)	Saturated zone	1/05/2017	-	0.44	-	70	-	-	97	460	0.11
R-20	Well 15 (468 m)	Saturated zone	1/05/2017	14.97	0.43	211	109	_	_	144	597	0.07
R-21	Well 15 (468 m)	Saturated zone	1/05/2017	_	0.43	_	112	-	_	147	593	0.07
R-24	Well 16	Saturated zone	1/05/2017	-	0.49	186	96	_	_	126	530	0.16
R-25	Well 16	Saturated zone	1/05/2017	_	0.49	_	93	_	_	122	518	0.17
1	Elder Creek	Stream	1/05/2017	28.29	0.12	251	59	14	247	138	239	0.07
5	Elder Creek	Stream	1/07/2017	28.90	0.12	246	62	14	247	138	234	0.05
7	Elder Creek	Stream	1/07/2017	28.68	0.11	226	54	13	217	121	219	0.12
9	Elder Creek	Stream	1/07/2017	28.61	0.11	230	53	14	222	124	216	0.12
11	Elder Creek	Stream	1/08/2017	28.30	0.12	229	56	14	220	122	214	0.10
MK4	By Well 7 <sup>b</sup>	Bedrock	1/08/2017	-0.57	7.76	729	_	627	_	739	_	4766

<sup>&</sup>lt;sup>a</sup> VMS and well samples are annotated with a corresponding depth and wellhead elevation, respectively. The depths reported for the VMS ports are the averages of sampling depth intervals relative to the wellhead (Tune et al., 2020).

**Table 2**Thermodynamic and kinetic rate parameters for Li-bearing minerals.

Mineral	Chemical formula <sup>a</sup>	$\log(K_{\rm eq,298K})^{\rm b}$	$\log(k_{298\text{ K},\text{pH}=7})^{c}$
Smectite	$Ca_{0.025}Na_{0.1}K_{0.2}Fe_{0.5}^{+2}Fe_{0.2}^{+3}Mg_{1.144112}^{-7}Li_{0.010892}^{-6}Li_{0.000884}Al_{1.25}Si_{3.5}(H_2O)_{12}$	17.42	-12.78
Smectite (isotopically light)	$Ca_{0.025}Na_{0.1}K_{0.2}Fe_{0.5}^{+2}Fe_{0.2}^{+3}Mg_{1.144112}{}^{7}Li_{0.010883}{}^{6}Li_{0.000893}Al_{1.25}Si_{3.5}(H_{2}O)_{12}$	17.42	-12.78
<sup>7</sup> Smectite (batch model)	$Ca_{0.025} Na_{0.1} K_{0.2} Fe_{0.5}^{+2} Fe_{0.2}^{+3} Mg_{1.144112}{}^{7} Li_{0.011776} Al_{1.25} Si_{3.5} (H_{2} O)_{12}$	17.42	-12.78
<sup>6</sup> Smectite (batch model)	$Ca_{0.025} Na_{0.1} K_{0.2} Fe_{0.5}^{+2} Fe_{0.2}^{+3} Mg_{1.144112}{}^{6} Li_{0.011776} Al_{1.25} Si_{3.5} (H_{2}O)_{12}$	17.42	-12.7727 <sup>e</sup>
<sup>7</sup> Kaolinite	$Al_{1.9997}^{7}Li_{0.0009}Si_{2}O_{5}(OH)_{4}$	6.81	-13.18
<sup>6</sup> Kaolinite	$Al_{1.9997}^{6}Li_{0.0009}Si_{2}O_{5}(OH)_{4}$	6.81	-13.1765 <sup>e</sup>
Kaolinite (batch model)	$Al_{1.9997}^{7}Li_{8.3245E-04}^{6}Li_{6.755E-05}Si_{2}O_{5}(OH)_{4}$	6.81	-13.18
<sup>7</sup> Illite	$K_{0.6}Mg_{0.24872}^{-7}Li_{0.00256}Al_{2.3}Si_{3.5}O_{10}(OH)_2$	9.02	-11.4 <sup>d</sup>
<sup>6</sup> Illite	$K_{0.6}Mg_{0.24872}{}^6Li_{0.00256}Al_{2.3}Si_{3.5}O_{10}(OH)_2$	9.02	-11.3894 <sup>e</sup>

<sup>&</sup>lt;sup>a</sup> The amount of total Li in each mineral is based on the Li/Mg and Li/Al ratios discussed in Supplementary Text S1.3. The partitioning of Li isotopes in non-fractionating phases (i.e., smectite in the vadose zone reactive transport model and kaolinite in the saturated zone batch model) reflects the  $\delta^7$ Li of that mineral.

<sup>&</sup>lt;sup>b</sup> Sample taken at an outcrop along path by Well 7.

<sup>&</sup>lt;sup>b</sup> Equilibrium constants are from the EQ3/6 database (Wolery et al., 1990).

<sup>&</sup>lt;sup>c</sup> Kinetic rate constants are from compilation of Palandri and Kharaka (2004) (unless individually annotated) and expressed in units of mol/m²/s.

<sup>&</sup>lt;sup>d</sup> Based on model validation against Li analyses (subsection 4.2 and subsubsection 5.1.1).

<sup>&</sup>lt;sup>e</sup> This study. The rate constants of <sup>6</sup>Li-bearing phases are offset from those of the <sup>7</sup>Li endmembers to implement a fractionation factor during mineral precipitation (i.e.,  $\alpha = {}^7k/{}^6k$ ).

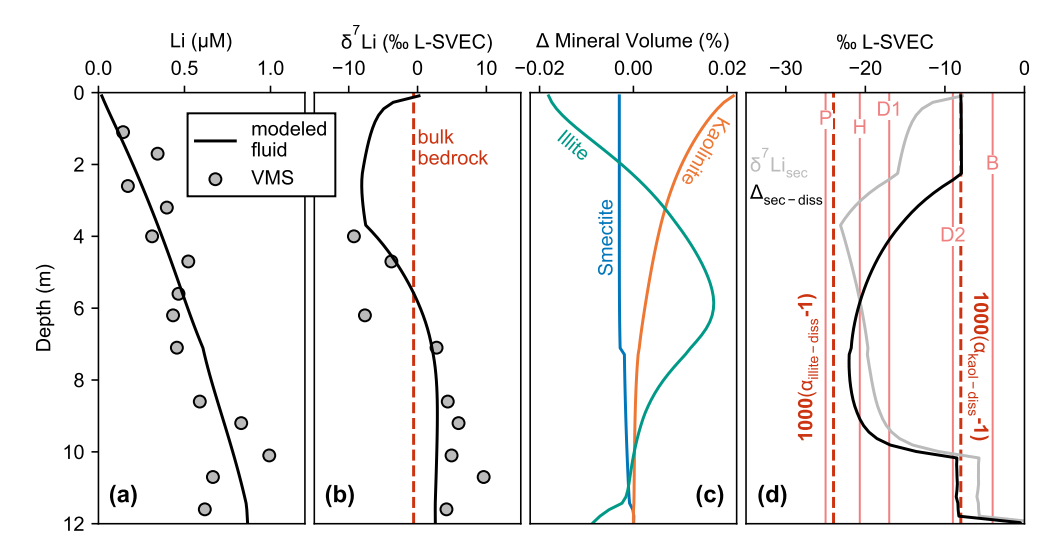


Fig. 4. Observations (circles) and reactive transport modeling results (solid lines) of dissolved Li concentrations (a) and isotopic signatures (b) of VMS samples in the vadose zone. In panel (b), the isotopic composition of the shale protolith is also marked as a red dashed line. Panel (c) shows simulated changes in mineral volume of Li-bearing phases with depth after five complete pore volume flushes (subsubsection 5.1.1). The estimated Li isotopic composition for a new bulk secondary phase  $\delta^7 \text{Li}_{\text{sec}}$ , and 'effective' isotopic fractionation between the new bulk secondary phase and fluid,  $\Delta_{\text{sec-diss}}$  (=  $\delta^7 \text{Li}_{\text{sec}}$  -  $\delta^7 \text{Li}_{\text{diss}}$ ; Eqn. (5)), are shown in panel (d) as solid gray and black lines, respectively. The dashed red vertical lines represent the fractionation factors for illite and kaolinite assigned to the model (to a close approximation,  $1000(\alpha_{\text{sec-diss}} - 1) \approx \Delta_{\text{sec-diss}}$ ), whereas the lighter red, solid vertical lines denote some of the  $\Delta_{\text{sec-diss}}$  values observed across different sites (B = Rayleigh fit for Brahmaputra River, Bagard et al., 2015; D1 = linear fit in Dellinger et al., 2015; D2 = Rayleigh fit in Dellinger et al., 2015; H = Rayleigh fit for Congo River, Henchiri et al., 2016; P = median from range of batch fits for the Ganges River, Pogge von Strandmann et al., 2017).

resent are detailed in the supplement (Supplementary Text S1.4). A fractionation factor for smectite is unnecessary as this phase remains undersaturated across the domain.

We emphasize that the modeled outputs emerge from forward simulations based on a set of parameters (flow rates, thermodynamic data, kinetic rate constants, solid-phase and aqueous major element geochemistry, mineral abundance, and specific surface areas) that is independently constrained by field observations and laboratory experiments (Wang, 2019; Gu et al., 2020). In the present study, only two relevant parameters are adjusted based on model validation against Li analyses: the clay isotope composition in the shallow subsurface and the kinetic rate constant for illite precipitation. Overall, this approach expands upon analytical models that do not explicitly account for the distribution of multiple minerals and aqueous species (e.g., Bohlin and Bickle, 2019; Lemarchand et al., 2010; Pogge von Strandmann et al., 2014) and numerical models that were not grounded by direct observations (e.g., Wanner et al., 2014).

#### 4. Results

#### 4.1. Li signatures

Dissolved Li concentrations and  $\delta^7 \text{Li}$  values across the vadose zone generally increase with depth (Fig. 4a-b). Notably, the sample volume obtained from some shallow VMS ports did not yield sufficient Li for isotope analysis. Li concentration profiles collected from both VMS-A and VMS-B behave similarly, with initial values of 0.17-0.34  $\mu$ M progressively increasing by as much as a factor of six to 0.82-0.98  $\mu$ M roughly 10 m below land surface (Table 1). VMS fluids are generally defined by a +14 to +18% shift with depth from the isotopically lightest samples (-7.7% VMS-A, -9.2% VMS-B) at shallow depths. In the analysis of vadose zone fluids, we omit the inclusion of any samples from ports that were fully saturated and thus located below the water table.

Measured Li concentrations and isotopic compositions vary substantially among the groundwater wells ([Li]  $=0.39\text{-}82~\mu\text{M};~\delta^7\text{Li}=+10~\text{to}~+25\%$ ). In contrast, Elder Creek Li concentrations are lower ([Li]  $=0.11\text{-}0.12~\mu\text{M})$  and the isotope ratios are even more

positive and tightly clustered ( $\delta^7 \text{Li} = +28$  to +29%; Table 1). To further interpret these results, we apply a correction for atmospheric inputs and normalize the Li concentrations to those of Na to account for dilution (Supplementary Text S2). There is a general decrease in the Li/Na ratio of groundwater (sampled from wells) downslope from ridge to stream, ranging from 5 to 0.58 (Fig. 5). The  $\delta^7 \text{Li}$  values similarly appear to vary systematically across the hillslope, from upslope wells (+13 to +15‰) to stream (+28 to +29‰), broadly increasing by +15 to +16‰.

Samples collected from the deepest VMS ports (>12 m) yield a set of shallow groundwater observations (Fig. 6). Relative to the range of Li compositions highlighted thus far, these samples show isotopic values (+8.9 to +17‰) that are intermediate between the unsaturated VMS and the groundwater wells, yet are characterized by uniquely elevated Li concentrations (0.64-2.8  $\mu$ M) (Table 1) and a wide range of Li/Na ratios. Two samples (A10 and B10) yield Li/Na ratios (2.7 and 3.1  $\mu$ M/mM) comparable to those of other saturated zone waters. In comparison, a second pair of samples (A9 and B9) exhibit values much higher than any other samples recorded in the study (7.5 and 18  $\mu$ M/mM).

#### 4.2. Model results

The vadose zone reactive transport model captures the general behavior of the Li solutes (Fig. 4a), reflecting the observed increase in concentration as a function of depth as the profile reaches a maximum value of  $\sim 0.87~\mu M$  at 12 m. As mentioned in subsection 3.3, two parameters were modified after incorporation of Li into the pre-existing Wang (2019) model to achieve agreement between simulated and measured Li isotopic profiles. First, reproducing the isotopically light fluid values measured in the depth profile was not possible using a balance between infiltrating rainwater ( $\delta^7 \text{Li of} + 31\%$ ) and dissolution of a bulk bedrock composition ( $\delta^7 \text{Li} = -0.57\%$ ), particularly given the enrichment of <sup>7</sup>Li in the fluid phase caused by fractionating secondary mineral growth. Therefore, we recognize that over the development of this weathering profile, the accumulation of secondary clays principally at shallow depths must result in a correspondingly negative solid-phase isotope ratio near the top of the profile. To honor this

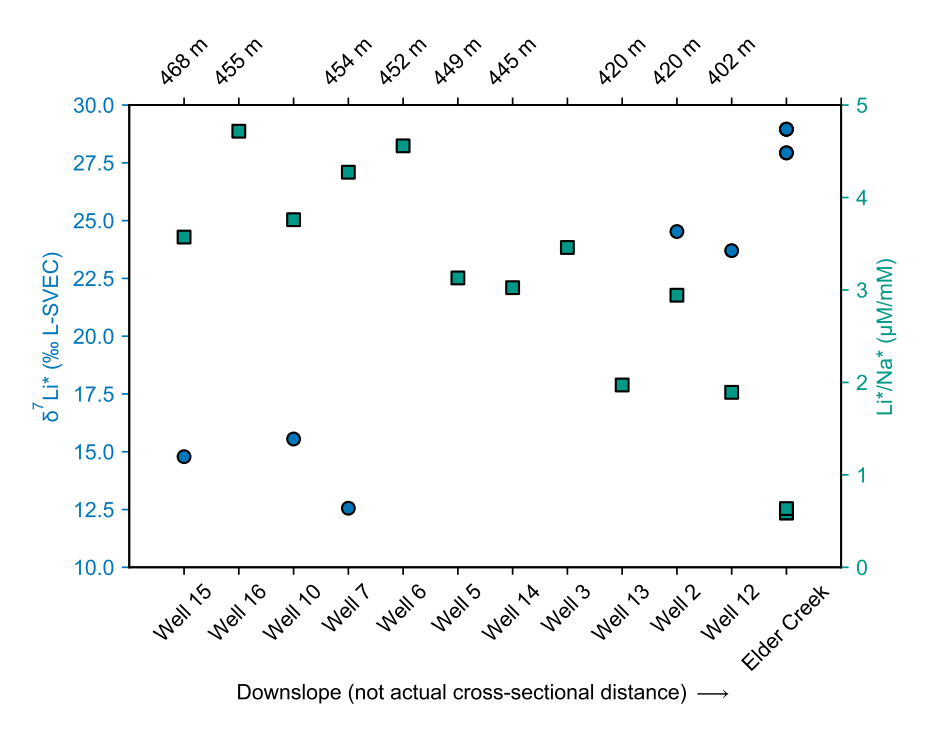


**Fig. 5.** Spatial distribution of fluid isotope ratios (blue circles) and dissolved lithium relative to dissolved sodium (Li\*/Na\* ratio; green squares) in the saturated zone. The wells do not directly lie along a transect, but are illustrated by their relative position and elevation across the Rivendell (Fig. 3). The stars (\*) indicate that molar concentrations and isotope ratios are corrected for atmospheric input (Supplementary Text S2).

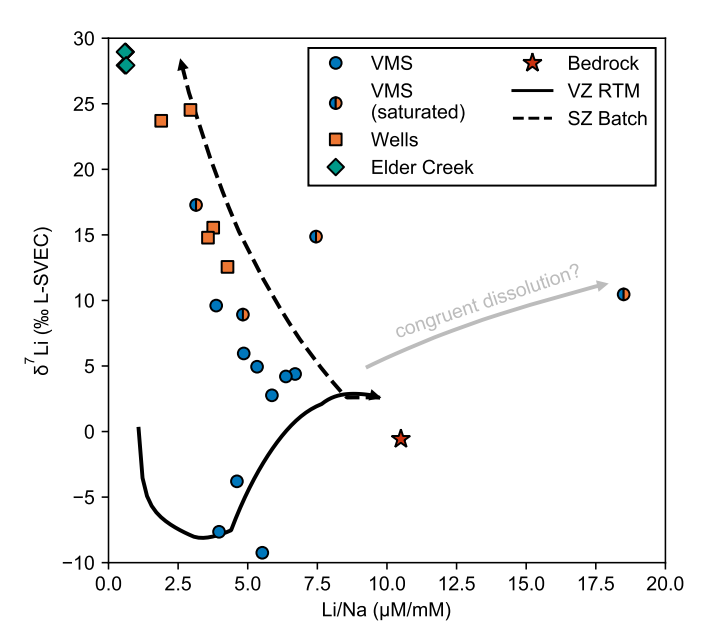


**Fig. 6.** Li/Na ratios and isotope signatures of VMS, well, and Elder Creek waters and the representative bulk bedrock sample. Concentrations and isotope ratios of well and Elder Creek samples are corrected for atmospheric input (Supplementary Text S2). Results of the vadose zone reactive transport model (solid) and the saturated zone batch-reactor model (dashed) are represented by black lines. An inferred trend for congruent dissolution is in gray. The vadose zone model faithfully reproduces Li concentrations with depth (Fig. 4a), although these trends are largely obscured when normalized to Na concentrations. This normalization alleviates variability in the measured data as a result of dilution (Supplementary Text S2). A version of this figure illustrating a direct comparison between modeled and observed Li concentrations is given in the supplement (Supplementary Fig. S1).

gradient, we adjust the composition of the dissolved Li sources above 4 m (i.e., partially dissolving smectite and illite) to -12% (Fig. 4b). Without this adjustment, modeled fluid  $\delta^7$ Li values result in a flat profile that overestimates all of the observed data above 8 m and underestimates those beneath this portion of the domain

(Supplementary Fig. S2). Such negative shallow solid-phase values have been observed for clay-rich soil in the Quiock Creek catchment in Guadeloupe, France (-13.5%; Clergue et al., 2015), and for saprolite along a weathering sequence from the Cayce diabase in South Carolina, USA (-20%); Rudnick et al., 2004). A gradient characterized by isotopically light signatures near the surface and increasing values with depth approaching the protolith composition has been observed in the solid-phase  $\delta^7$ Li of other weathering profiles of comparable scale (Kısakürek et al., 2004; Liu et al., 2013). At Shale Hills in northeastern USA, the bulk signatures of shallow soil (-1.1%) and shale bedrock (-1.6%) are heavier than what is estimated for the secondary mineral constituents (as low as -5.7%; Steinhoefel et al., 2021). Hence, this model adjustment also accounts for the possibility that low fluid  $\delta^7 \text{Li}$  can result from solid material with a crust-like ( $+0.6 \pm 0.6\%$ ; Sauzéat et al., 2015) bulk  $\delta^7$ Li signature via preferential dissolution of <sup>6</sup>Lidepleted secondary minerals (Lemarchand et al., 2010; Pistiner and Henderson, 2003) and emerging evidence suggesting potential isotopic fractionation during clay dissolution that would result in the preferential release of <sup>6</sup>Li to solution (Zhang et al., 2021b).

The second parameter adjustment is an increase in the rate constant of illite from  $10^{-14.8}$  to  $10^{-11.4}$  mol/m²/s (Table 2), which is comparable to values used in other shale-based reactive transport models  $(10^{-11.0}$ - $10^{-10.98}$  mol/m²/s; Li et al., 2020; Phan et al., 2018). This increase is essential to achieving the relatively large positive shift in  $\delta^7$ Li across the deep portions the profile (Supplementary Fig. S2). Critically, we emphasize that these updates do not significantly alter the replicability of the major cation profiles reported in Wang (2019) (Supplementary Fig. S3), highlighting the utility of dissolved Li isotope ratios in parsing silicate weathering processes beyond what is resolvable through major cation chemistry. The implications of this parameter tuning are discussed in further detail below (subsection 5.1).

As a demonstration of the mass balance principles underlying the simulation results, we note that the modeled fluid  $\delta^7 {\rm Li}$  profile starts near 0% despite the implementation of a +31% upper boundary condition for the dissolved phase (Fig. 4b). Such a rapid

drop highlights the strong influence the solid phase exerts on dissolved Li values as dilute rainwater enters the subsurface. With further depth, the simulated  $\delta^7 \text{Li}$  values follow a sharp decrease to values near -8%, reflecting the adjusted initial model condition of isotopically light clay assumed over the upper section of the domain. Although the Li sources to the solution in this shallow layer are -12%, the aqueous phase does not reach such a negative value. Thus, the preservation of an isotopically heavy fluid relative to the surrounding regolith in this upper section of the domain is a first indication that isotope fractionation via secondary mineral formation is playing an important role at these depths (discussed further in subsubsection 5.1.1). Across the deeper sections of the model, the trend of the VMS observations is mimicked by the dissolved  $\delta^7$ Li simulation, which asymptotically approaches a single value (+3\%) of  $\delta^7$ Li in the fluid phase. In the absence of isotopic fractionation associated with secondary mineral formation, the model faithfully returns a fluid approaching the bedrock  $\delta^7$ Li value at depth (Supplementary Text S3.1). Further sensitivity analysis of individual fractionation factors and flow rates are also offered in the supplement (Supplementary Texts S3.1 and S3.2).

In the saturated zone, we run an extended simulation forward in time (called "SZ batch" in Fig. 6; described in subsection 3.3) starting from the composition corresponding to the fluid at the base of the vadose zone reactive transport simulation (called "VZ RTM" in Fig. 6). Results show that the trajectory of both dissolved  $\delta^7 {\rm Li}$  and Li/Na ratios reproduce the observed progression of the Li isotope composition from the deepest unsaturated VMS signatures to those observed in the wells and ultimately in Elder Creek (Fig. 6).

#### 5. Discussion

5.1. The weathering reactions within a hillslope as recorded by dissolved lithium and its isotopes

#### 5.1.1. Characteristic silicate weathering reactions

A principal objective of the isotope-enabled reactive transport framework is to deconvolve the characteristic silicate weathering reactions that govern the Critical Zone structure and produce the fluid chemical compositions that are exported to the drainage network. The dissolved Li concentrations and stable isotope ratios (Figs. 4a-b) are generated as a result of simultaneous dissolution and precipitation of multiple Li-bearing phases (Fig. 4c). Modeled changes in mineral volume (Fig. 4c) are calculated by differencing the results between an initial simulation where quasi-steady state is achieved (Supplementary Text S1.1) and a subsequent simulation lasting for an additional 6 yr reflecting multiple passages of water ( $\sim$ 5 renewal of total pore volume) through the domain. Based on these relative rates of mineral alteration, we observe that smectite dissolves at a relatively constant rate across the upper 7 m, below which it progressively trends to an infinitesimal relative change in mineral volume. In the shallowest portion of the depth profile, new secondary clay formation is dominated by kaolinite, but is overtaken by illite formation at around 2.4 m. Like smectite, there is virtually no change in kaolinite mineral volume near the bottom of the domain. In comparison, the behavior of illite is characterized by shallow and deep intervals of dissolution and an intermediate zone of precipitation that is maximized at  $\sim$ 6 m. This forward model results in dynamic dissolution-precipitation conditions (Fig. 4c) that are in agreement with the thermodynamic stabilities of clay minerals (Drever, 1988; Supplementary Fig. S7) and the mineralogy generally observed at Rivendell (Gu et al., 2020). Notably, the modeled dissolution of illite in the upper 2.4 m of the profile is consistent with observed relative depletion of the mineral in multiple bulk soil samples (Gu et al., 2020).

The model reproducibility of the measured fluid  $\delta^7 {\rm Li}$  signatures (Fig. 4b) demonstrates the sensitivity of the reactive transport signatures of Li to the relative rates of clay formation. This relationship is underscored by the single instance in which we needed to increase the kinetic rate constant of illite (or equivalently increase the reactive surface area of illite) in order to achieve sufficient Li isotope fractionation to reproduce the dissolved isotopic signatures below the shallowest layers of the profile (subsection 4.2). This adjustment provided a critical improvement to the isotope model and exerted a negligible effect on the modeled cation concentrations (Supplementary Fig. S3), highlighting the sensitivity of isotope ratios to these parameter values and to the type of clay precipitating.

As a result, the model generates a bottom-up prediction of the solid phase mineralogy that shifts from illite- to kaolinite-dominated secondary mineral formation reflecting the transition from early to later (or deeper to shallower) stages of silicate weathering. This result is consistent with observations of abundant kaolinite at the top of mature weathering profiles (e.g., Murphy et al., 1998; White et al., 2001) due to the relative insolubility of Al in its structure. In our simulations, as with prior work (Maher and von Blanckenburg, 2016), the location of maximum kaolinite accumulation is dictated by the balance between saturation state and flow rate. Such parallels highlight the enhanced utility of Li isotopes as a potent tracer of silicate weathering pathways in a reactive transport model.

#### 5.1.2. Insights into apparent Li isotope fractionation

We use our modeling framework to constrain what we hereafter refer to as an 'effective' Li isotope fractionation based on the secondary mineral phases forming through space and time. Such effective isotope fractionation stems from the relative roles of multiple fractionating processes impacting the Li isotope distribution in hillslopes, each with their own individual or 'intrinsic' isotope fractionation factor. This is obtained from our model results by tracking the isotopic composition of a representative newly forming bulk secondary solid weighted by the amount of Li incorporated into each contributing mineral

$$\delta^{7} \operatorname{Li}_{\operatorname{sec}} (\%_{0}) = \sum_{i}^{N} f_{i}^{\operatorname{Li}} \left( \frac{\frac{{}^{7} V_{i}}{{}^{6} \operatorname{Li}}}{\frac{{}^{7} \operatorname{Li}}{{}^{6} \operatorname{Li}} \operatorname{L-SVEC}} - 1 \right) \times 1000, \tag{2}$$

where  ${}^{7}V_{i}$  and  ${}^{6}V_{i}$  each correspond to the new mineral volume (as defined in subsubsection 5.1.1) of the  ${}^{7}\text{Li}$  and  ${}^{6}\text{Li}$  solid solution endmembers for N precipitating mineral(s) and

$$f_i^{\text{Li}} = \frac{n_i^{\text{Li}}}{\sum n_i^{\text{Li}}},\tag{3}$$

given

$$n_i^{\text{Li}} = \frac{(^7V_i + ^6V_i)x_i}{V_i^m},\tag{4}$$

such that  $x_i$  is the number of moles of Li per mole of mineral and  $V_i^m$  is the mineral molar volume. The bulk secondary solid is isotopically lightest at depths where kaolinite and illite formation are simultaneous (Figs. 4c and 4d).  $\delta^7 \text{Li}_{\text{sec}}$  trends toward heavier values deeper in the domain, following the progressive enrichment of the fluid phase from which these minerals are formed, but the value of  $\delta^7 \text{Li}_{\text{sec}}$  never reaches the measured bulk bedrock value of -0.57%. With this information, the effective isotopic fractionation between the newly formed bulk secondary solid and the dissolved phase,  $\Delta_{\text{sec-diss}}$ , can be calculated as

$$\Delta_{\text{sec-diss}} = \delta^7 \text{Li}_{\text{sec}} - \delta^7 \text{Li}_{\text{diss}},\tag{5}$$

where  $\delta^7 \text{Li}_{\text{diss}}$  corresponds to the isotopic composition of the dissolved phase.

In the shallow and deep portions of the profile where the formation of new secondary phases only occurs as kaolinite (Fig. 4c), the value of  $\Delta_{\rm sec\text{-}diss}$  is -8%, reflecting the  $\alpha_{\rm kaolinite\text{-}diss}$  of 0.992 prescribed to the model (Fig. 4d). Across the depths dominated by illite formation, the  $\Delta_{\rm sec\text{-}diss}$  values approach peak fractionation at -19%, which is only achieved when changes in kaolinite mineral volume become minimal at  $\sim\!\!8$  m. This maximum  $\Delta_{\rm sec\text{-}diss}$  never reaches the assigned  $\alpha_{\rm illite\text{-}diss}=0.976$ . At the very bottom of the domain, virtually no secondary minerals are precipitated and thus no fractionation occurs ( $\Delta_{\rm sec\text{-}diss}=0\%$ ). These results illustrate how the individual intrinsic fractionation factors imposed for kaolinite and illite formation manifest in the fluid- and solid-phase isotope signatures produced by the simulation.

The variable  $\Delta_{\text{sec-diss}}$  that emerges from our model demonstrates the extraordinary sensitivity of Li isotope fractionation to the contemporaneous rates and solubilities of multiple secondary mineral phases. Intermediate  $\Delta_{\text{sec-diss}}$  values in the profile are produced due to the competition between the unique fractionation factors associated with kaolinite and illite formation. This outcome indicates that the observed range of effective isotopic fractionation (defined by Eqn. (5)) is a consequence of the predominant secondary mineral forming in the subsurface as a function of depth (or time), suggesting that the variability of dissolved  $\delta^7$ Li signatures within a given field site may reflect a shift between or among multiple secondary phases governing Li isotope partitioning (e.g., Murphy et al., 2019). Furthermore, the formation of a variety of secondary mineral assemblages should contribute to the wide range of  $\Delta_{\text{sec-diss}}$  values observed across disparate field sites and regions (Fig. 4d). Our model illustrates that a  $\Delta_{\text{sec-diss}}$  variation of as much as 11% can be produced as a result of a simple balance between formation of two contemporaneous secondary phases with unique intrinsic fractionation fac-

Additional factors may influence  $\delta^7$ Li signatures in fluid samples taken from natural systems. For example, isotope fractionation factors commonly appear to be 'muted' or dampened in field-scale observations relative to intrinsic values produced in closed systems typical of laboratory studies (e.g., Berna et al., 2010). The increased length scale of spatial averaging over which samples are collected in heterogeneous natural systems (e.g., large rivers; Gaillardet et al., 1999; Meybeck, 1987; Stallard and Edmond, 1983) has been proposed to cause this isotopic discrepancy (Druhan and Maher, 2017). This effect may explain why the fractionation factors used to describe the evolution of  $\delta^7 \text{Li}$  in the rivers ( $\alpha_{\text{sec-diss}}$  of 0.995 and 0.996) appeared muted relative to the value fitted to shallow groundwaters ( $\alpha_{\text{sec-diss}} = 0.991$ ) in the Ganges-Brahmaputra floodplain (Bagard et al., 2015). In contrast, relatively small length scales of observation, such as the  $\delta^7 \text{Li}$  of soil samples across a ~13-cm profile in the Quiock Creek illustrate a maximum range of  $\alpha_{\text{sec-diss}} = 0.970 - 0.973$  (Clergue et al., 2015) that is comparable to the intrinsic  $\alpha_{gibbsite-diss} = 0.975$  experimentally determined by Millot and Girard (2007). In total, these comparisons show the potential of forward reactive transport modeling approaches such as the one used here to offer a more realistic parsing of the distribution of multiple secondary phases within an open system. We show that this approach can predict effective isotopic fractionation factors between and among phases using a variety of pathways beyond the capabilities of simpler batch or Rayleigh models that require fitting of a single fractionation factor. This utility is vital to linking experimentally determined, intrinsic isotopic fractionation factors to the variability observed in natural systems.

#### 5.2. Evolution of silicate weathering from hillslopes to rivers

Below the water table, fluids collected from traditional wells allow us to constrain geochemical evolution of groundwater from the top of the hillslope to the base where it discharges to Elder Creek. Along this profile, dissolved  $\delta^7 \text{Li}$  signatures trend towards heavier values with a corresponding decrease in Li/Na ratios downslope (Figs. 5 and 6). These observations suggest that the pathways of secondary mineral formation that fractionate Li isotopes and deplete Li concentrations continue beyond the vadose zone and into the saturated zone as groundwater migrates laterally downslope. We expand our vadose zone reactive transport model to explore these saturated conditions (subsection 3.3), finding that the major geochemical reactions defining this continued evolution are the dissolution of kaolinite and the precipitation of illite and, to a much lesser extent, smectite (Supplementary Fig. S8). To reflect these geochemical changes, the saturated zone model is adjusted to include isotopic fractionation during precipitation of smectite on the order of  $\alpha_{\rm smectite-diss} =$  0.9834 (Table 2; Hindshaw et al., 2019; Supplementary Text S1.4). In conjunction with the vadose zone simulations, these model results indicate the top-down progression of silicate weathering beginning in the vadose zone and continuing across the water table and within the saturated zone, ultimately reaching the stream at the base of the hillslope. This reaction pathway is initiated in our batch model simulation by the formation of kaolinite that is only stable under near-surface conditions and progresses below the water table through the eventual shift to precipitation of metastable clays, like illite and smectite. which can persist at depth due to gradual solute enrichment and favorable alkaline conditions (e.g., Eberl, 1984; Langmuir, 1997). From the base of the Critical Zone, the characteristic silicate weathering reactions in the saturated zone mark the initial stages of the bottom-up maturation of the shale bedrock.

Based on elemental compositions alone, the vadose zone and well waters are largely indistinguishable. Prior studies have interpreted Rivendell groundwater solute concentrations as evidence for a lack of appreciable silicate weathering below the water table (e.g., Kim et al., 2014, 2017). With the new constraints afforded by  $\delta^7$ Li signatures, the modeled progression of isotopic composition highlights the continuity of silicate weathering through the vadose zone and into the saturated zone (Fig. 6). The high silicate weathering rates of the vadose zone are driven by the influx of reactive meteoric fluids. Below the water table, silicate weathering is sustained through the combination of contact between laterally-flowing waters and unweathered bedrock and of the evacuation of chemically saturated groundwaters via drainage to Elder Creek. This weathering regime in the saturated zone appears to be masked in solute concentrations, but is now apparent through the lens of Li stable isotopes.

While the saturated zone model offers only an approximate translation between time and the highly variable flow paths of Rivendell, the point at which the simulation achieves  $\delta^7$ Li enrichment that appropriately represents the isotope ratios observed in the wells at the base of the hillslope ( $\sim+25\%$ ): Figs. 5 and 6) places some constraint on the solute load derived from silicate weathering via lateral drainage of the hillslope. Dissolved silicon is used as a metric given its sensitivity to both solubilization and precipitation reactions that occur during silicate weathering. We find that fluid concentrations reach 0.48 mM over the depth interval from infiltration to the base of the vadose zone, and further increased to 1.2 mM upon reaching the base of the hillslope. Although these figures only constitute a first-order estimate of net silicate weathering rates, this comparison suggests that comparable weathering-derived solute masses are generated in the saturated zone versus above the water table.

The simulation is not able to capture the small subset of uniquely high Li concentrations (as much as  $\sim$ 2.7  $\mu$ M) in some of the deepest VMS ports (Fig. 6 and Supplementary Fig. S1). As noted earlier, these deep VMS ports became water-saturated and thus reflect shallow groundwater samples, which returned two measurements with low Li/Na ratios (characteristic of the silicate weathering conditions that influence the deeper groundwater wells and stream water) and two other measurements with anomalously high Li/Na ratios. In particular, the most Li-concentrated sample yielded a Li/Na ratio (18 µM/mM) almost double that of the bedrock (10.6 µM/mM; Table 1), implying that the amount of Li dissolved is in excess of what would be released from congruent dissolution. A closer inspection of the overall geochemical composition via multivariate analysis (Supplementary Fig. S9) reveals that all major weathering-derived cations are also enriched in these two shallow groundwater samples while the Li isotopes remain consistent with other saturated zone samples. Furthermore, the depth interval (13.1-13.7 m) of these cation-enriched fluids corresponds to the location of the base of the weathering front (15 m) inferred from solid-phase elemental composition for a nearby borehole at Well 10 (Fig. 3; Gu et al., 2020). The fluctuation of the water table in this zone may facilitate periodic introduction of reactive gases and rapid delivery of relatively chemically undersaturated waters that favor dissolution of the most soluble minerals (including Li-rich chlorite; Gu et al., 2020) composing the fresh shale protolith. Hence, the shallowest depths of the saturated zone may be an intermittent hotspot of heightened weathering rates, which releases elevated cation concentrations and impart a bedrock-like  $\delta^7$ Li signature to fluids.

#### 5.3. Implications for interpretation of Li isotope signatures in rivers

The systematic evolution of Li signatures through the Rivendell hillslope allows us to test the hypotheses proposed by Bouchez et al. (2013) for the relationship between  $\delta^7 \text{Li}$  and regolith residence time, which has been used to interpret the  $\delta^7$ Li signatures of major rivers (e.g., Dellinger et al., 2015; Wang et al., 2015) (Fig. 1). The reactive transport of Li through the compartments of the Rivendell hillslope creates conditions in which fluid experiences each of the three endmember processes (section 1: processes 1, 2 and 3) in the interval between infiltration and discharge. In the shallow vadose zone (0-2.4 m depth, Fig. 4), high weathering intensity is facilitated by the infiltration of meteoric water charged with reactive gases that causes dissolution of cation-rich and Libearing clays, like illite and smectite, and thus low  $\delta^7$ Li values. These shallow vadose zone conditions are thus consistent with supply-limited weathering regimes (process 3), where the dissolution of isotopically depleted, weathered material is interpreted to explain low  $\delta^7$ Li and low Li concentrations observed in riverine samples (Dellinger et al., 2015). The hypothesized hotspot of rapid dissolution of bedrock at the top of the Rivendell saturated zone (Figs. 6 and Supplementary Fig. S9) is similarly characteristic of a low-weathering intensity regime (process 1) wherein fresh material is supplied at a faster rate than secondary mineral formation occurs. This general pattern of elemental depletion associated with the top of the saturated zone (or the depth at which bedrock becomes fractured and open to fluid circulation) is common (e.g., Anderson et al., 2002; Jin et al., 2010; Uhlig and von Blanckenburg, 2019). Because these conditions elicit more congruent weathering, isotopic fractionation is relatively minimal and concentrations are the highest, as observed in this study and previous work (Dellinger et al., 2015; Huh et al., 2001; Misra and Froelich, 2012). At catchment scales, the intermediate weathering intensity endmember is such that weathering and erosion in a system do not significantly outpace one another (process 2). Analogously, the isotopic ratios of some waters in the saturated zone can approach high  $\delta^7$ Li values while maintaining moderate Li concentrations due to coupled pathways of silicate weathering driven by the relative solubilities of simultaneously dissolving and forming clays. Critically, this intermediate-depth reactivity is enhanced by the delivery of organics deep below soil via the roots of the mature forest ecosystem, which sustains a persistent source of respired CO<sub>2</sub> driving weathering (Tune et al., 2020). Similarly, the highest increase in  $\delta^7 \text{Li}$ , comparable Li concentrations, and a transition from kaolinite- to illite-dominant precipitation observed deeper in the vadose zone ( $\geq 2$  m depth, Fig. 4) depict an increasingly incongruent weathering pattern.

Our observations and the parallels to other studies highlight the capacity for any hillslope of the basic structure represented at Rivendell to reflect the entirety of the weathering intensity –  $\delta^7 {\rm Li}$  relationships inferred previously across disparate regions based on solute fluxes of large rivers. The large shifts and predictive patterns in Li signatures we quantify across a small, first-order hillslope record generation and transport of solutes through a structured set of compartments each hosting unique conditions of silicate weathering.

#### 6. Conclusions

We find that in first-order hillslopes, silicate weathering is continuous as meteoric water infiltrating through the vadose zone is transferred to groundwater and ultimately discharged to streams. This work also highlights the enhanced sensitivity afforded by combining Li isotopes and concentrations in effectively capturing unique instances of dissolution-precipitation processes (e.g., secondary mineral neoformation, clay transformation, congruent dissolution) that define a range of silicate weathering regimes. In particular, heavy dissolved Li isotope signatures that occur near the bottom of the weathering profile trace the formation of secondary minerals and, thus, active weathering. The light dissolved Li isotope signatures, such as those measured toward the top of the regolith profile, reflect clay dissolution and, hence, the chemical disaggregation of previously weathered material. Elevated Li concentrations within the zone of water table fluctuation mark the congruent dissolution of bedrock. The heavy isotope ratios at the base of the hillslope suggest the continuation of silicate weathering below the water table, which combines with the Li signature of the vadose zone as an integrated export to the stream. This finding motivates the investigation of the seasonal relationship(s) between isotope ratio and discharge in low-order streams, which may offer a lens into the architecture of these weathering zones beyond what has been achieved through more common concentration-discharge dynamics.

#### **CRediT** authorship contribution statement

Jon K. Golla: Funding acquisition, Conceptualization, Investigation, Methodology, Software, Writing – original draft, Writing – review & editing. Marie L. Kuessner: Funding acquisition, Investigation, Methodology, Validation. Michael J. Henehan: Methodology, Resources, Validation, Writing – review & editing. Julien Bouchez: Funding acquisition, Conceptualization, Resources, Validation, Writing – review & editing. Daniella M. Rempe: Funding acquisition, Conceptualization, Resources, Writing – review & editing. Jennifer L. Druhan: Funding acquisition, Conceptualization, Methodology, Resources, Software, Writing – original draft, Writing – review & editing.

#### **Declaration of competing interest**

The authors declare that they have no known competing financial interests or personal relationships that could have appeared to influence the work reported in this paper.

#### Acknowledgements

This research was partially funded by the People Programme (Marie Curie Actions) of the European Union's Seventh Framework Programme FP7/2007-2013/ under REA agreement [608069] (ITN "IsoNose"), the IPGP multidisciplinary program PARI, and the Region île-de-France SESAME Grant No. 12015908. J.K.G. is supported by the National Science Foundation (NSF) Graduate Research Fellowship Program, M.L.K. was supported by a joint OZCAR (French CZO Network) - CZEN (Critical Zone Exploration Network) fellowship. J.K.G. and J.L.D. acknowledge funding support from NSF-EAR-2047318. The Eel River Critical Zone Observatory is supported by NSF-EAR-1331940. M.J.H. and M.L.K. thank Jutta Schlegel and Josefine Buhk for assistance in the laboratory. We thank Gunnar Reith and Will Speiser for help with sample collection. We are grateful to Friedhelm von Blanckenburg for providing helpful feedback on an earlier version of the manuscript. We thank editor Louis Derry, Philip Pogge von Strandmann, and an anonymous reviewer for their constructive comments.

#### Data availability statement

The source code for the CrunchFlow/CrunchTope software is available on Bitbucket (https://bitbucket.org/crunchflow). Please contact Dr. Jennifer Druhan (Assistant Professor at the University of Illinois at Urbana-Champaign) for more information about and access to the updated CrunchFlow/CrunchTope version used in this work, The associated model input files can be accessed on GitHub (https://github.com/jkgolla/ERCZOLithiumCrunchInput) and are archived on Zenodo (https://doi.org/10.5281/zenodo.4642871).

#### Appendix A. Supplementary material

Supplementary material related to this article can be found online at https://doi.org/10.1016/j.epsl.2021.116988.

#### References

- Ahnert, F., 1970. Functional relationships between denudation, relief, and uplift in large, mid-latitude drainage basins. Am. J. Sci. 268 (3), 243–263. https://doi.org/10.2475/ajs.268.3.243.
- Anderson, S.P., Dietrich, W.E., Brimhall, G.H., 2002. Weathering profiles, mass-balance analysis, and rates of solute loss: linkages between weathering and erosion in a small, steep catchment. Geol. Soc. Am. Bull. 114 (9), 1143–1158. https://doi.org/10.1130/0016-7606(2002)114<1143:WPMBAA>2.0.CO;2.
- Anderson, S.P., von Blanckenburg, F., White, A.F., 2007. Physical and chemical controls on the Critical Zone. Elements 3 (5), 315–319. https://doi.org/10.2113/gselements.3.5.315.
- Bagard, M.-L., West, A.J., Newman, K., Basu, A.R., 2015. Lithium isotope fractionation in the Ganges-Brahmaputra floodplain and implications for groundwater impact on seawater isotopic composition. Earth Planet. Sci. Lett. 432, 404–414. https:// doi.org/10.1016/j.epsl.2015.08.036.
- Berna, E.C., Johnson, T.M., Makdisi, R.S., Basu, A., 2010. Cr stable isotopes as indicators of Cr(VI) reduction in groundwater: a detailed time-series study of a point-source plume. Environ. Sci. Technol. 44 (3), 1043–1048. https://doi.org/10.1021/es902280s.
- Bohlin, M.S., Bickle, M.J., 2019. The reactive transport of Li as a monitor of weathering processes in kinetically limited weathering regimes. Earth Planet. Sci. Lett. 511, 233–243. https://doi.org/10.1016/j.epsl.2019.01.034.
- Bormann, F.H., Likens, G.E., 1967. Nutrient cycling. Science 155 (3761), 424–429. https://doi.org/10.1126/science.155.3761.424.
- Bouchez, J., von Blanckenburg, F., Schuessler, J.A., 2013. Modeling novel stable isotope ratios in the weathering zone. Am. J. Sci. 313 (4), 267–308. https://doi.org/10.2475/04.2013.01.
- Brantley, S.L., Lebedeva, M., 2011. Learning to read the chemistry of regolith to understand the Critical Zone. Annu. Rev. Earth Planet. Sci. 39 (1), 387–416. https://doi.org/10.1146/annurev-earth-040809-152321.
- Brimhall, G.H., Dietrich, W.E., 1987. Constitutive mass balance relations between chemical composition, volume, density, porosity, and strain in metasomatic hydrochemical systems: results on weathering and pedogenesis. Geochim. Cosmochim. Acta 51 (3), 567–587. https://doi.org/10.1016/0016-7037(87)90070-6.

- Burton, K.W., Vigier, N., 2012. Lithium isotopes as tracers in marine and terrestrial environments. In: Baskaran, M. (Ed.), Handbook of Environmental Isotope Geochemistry: Vol. I. Springer, Berlin, Heidelberg, pp. 41–59.
- Calmels, D., Galy, A., Hovius, N., Bickle, M., West, A.J., Chen, M.-C., Chapman, H., 2011. Contribution of deep groundwater to the weathering budget in a rapidly eroding mountain belt, Taiwan. Earth Planet. Sci. Lett. 303 (1), 48–58. https://doi.org/10.1016/j.epsl.2010.12.032.
- Clergue, C., Dellinger, M., Buss, H.L., Gaillardet, J., Benedetti, M.F., Dessert, C., 2015. Influence of atmospheric deposits and secondary minerals on Li isotopes budget in a highly weathered catchment, Guadeloupe (Lesser Antilles). Chem. Geol. 414, 28–41. https://doi.org/10.1016/j.chemgeo.2015.08.015.
- Dahan, O., Talby, R., Yechieli, Y., Adar, E., Lazarovitch, N., Enzel, Y., 2009. In situ monitoring of water percolation and solute transport using a vadose zone monitoring system. Vadose Zone J. 8 (4), 916–925. https://doi.org/10.2136/vzj2008.0134.
- Dellinger, M., Gaillardet, J., Bouchez, J., Calmels, D., Louvat, P., Dosseto, A., et al., 2015. Riverine Li isotope fractionation in the Amazon River basin controlled by the weathering regimes. Geochim. Cosmochim. Acta 164, 71–93. https://doi.org/ 10.1016/j.gca.2015.04.042.
- Drever, J.I., 1988. The Geochemistry of Natural Water. Pearson Education, Canada.
- Druhan, J.L., Maher, K., 2017. The influence of mixing on stable isotope ratios in porous media: a revised Rayleigh model. Water Resour. Res., 1101–1124. https://doi.org/10.1002/2016WR019666.
- Druhan, J.L., Steefel, C.I., Williams, K.H., DePaolo, D.J., 2013. Calcium isotope fractionation in groundwater: molecular scale processes influencing field scale behavior. Geochim. Cosmochim. Acta 119, 93–116. https://doi.org/10.1016/j.gca.2013.05.022
- Druhan, J.L., Fernandez, N., Wang, J., Dietrich, W.E., Rempe, D., 2017. Seasonal shifts in the solute ion ratios of vadose zone rock moisture from the Eel River Critical Zone Observatory. Acta Geochim. 36 (3), 385–388. https://doi.org/10.1007/s11631-017-0169-z.
- Eberl, D.D., 1984. Clay mineral formation and transformation in rocks and soils. Philos. Trans. R. Soc. Lond. Ser. A, Math. Phys. Sci. 311 (1517), 241–257. https://doi.org/10.1098/rsta.1984.0026.
- Flesch, G., Anderson Jr, A., Svec, H., 1973. A secondary isotopic standard for <sup>6</sup>Li/<sup>7</sup>Li determinations. Int. J. Mass Spectrom. Ion Phys. 12 (3), 265–272.
- Fuller, T.K., Perg, L.A., Willenbring, J.K., Lepper, K., 2009. Field evidence for climatedriven changes in sediment supply leading to strath terrace formation. Geology 37 (5), 467–470. https://doi.org/10.1130/G25487A.1.
- Gaillardet, J., Dupré, B., Louvat, P., Allègre, C.J., 1999. Global silicate weathering and CO<sub>2</sub> consumption rates deduced from the chemistry of large rivers. Chem. Geol. 159 (1), 3–30. https://doi.org/10.1016/S0009-2541(99)00031-5.
- Garrels, R., Mackenzie, F.T., 1971. Evolution of Sedimentary Rocks. Norton, New York. Gu, X., Rempe, D.M., Dietrich, W.E., West, A.J., Lin, T.-C., Jin, L., Brantley, S.L., 2020. Chemical reactions, porosity, and microfracturing in shale during weathering: the effect of erosion rate. Geochim. Cosmochim. Acta 269, 63–100. https://doi.org/10.1016/j.gca.2019.09.044.
- Henchiri, S., Gaillardet, J., Dellinger, M., Bouchez, J., Spencer, R.G.M., 2016. Riverine dissolved lithium isotopic signatures in low-relief central Africa and their link to weathering regimes. Geophys. Res. Lett. 43 (9), 4391–4399. https://doi.org/ 10.1002/2016GL067711.
- Hindshaw, R.S., Tosca, R., Goût, T.L., Farnan, I., Tosca, N.J., Tipper, E.T., 2019. Experimental constraints on Li isotope fractionation during clay formation. Geochim. Cosmochim. Acta 250, 219–237. https://doi.org/10.1016/j.gca.2019.02.015.
- Huh, Y., Chan, L.-H., Edmond, J.M., 2001. Lithium isotopes as a probe of weathering processes, Orinoco River. Earth Planet. Sci. Lett. 194 (1), 189–199. https://doi.org/10.1016/S0012-821X(01)00523-4.
- James, R.H., Palmer, M.R., 2000. The lithium isotope composition of international rock standards. Chem. Geol. 166 (3), 319–326. https://doi.org/10.1016/S0009-2541(99)00217-X.
- Jin, L., Ravella, R., Ketchum, B., Bierman, P.R., Heaney, P., White, T., Brantley, S.L., 2010. Mineral weathering and elemental transport during hillslope evolution at the Susquehanna/Shale Hills Critical Zone Observatory. Geochim. Cosmochim. Acta 74 (13), 3669–3691. https://doi.org/10.1016/j.gca.2010.03.036.
- Kim, H., Bishop, J.K.B., Dietrich, W.E., Fung, I.Y., 2014. Process dominance shift in solute chemistry as revealed by long-term high-frequency water chemistry observations of groundwater flowing through weathered argillite underlying a steep forested hillslope. Geochim. Cosmochim. Acta 140, 1–19. https:// doi.org/10.1016/j.gca.2014.05.011.
- Kim, H., Dietrich, W.E., Thurnhoffer, B.M., Bishop, J.K.B., Fung, I.Y., 2017. Controls on solute concentration-discharge relationships revealed by simultaneous hydrochemistry observations of hillslope runoff and stream flow: the importance of critical zone structure. Water Resour. Res. 53 (2), 1424–1443. https:// doi.org/10.1002/2016WR019722.
- Kısakürek, B., Widdowson, M., James, R.H., 2004. Behaviour of Li isotopes during continental weathering: the Bidar laterite profile, India. Chem. Geol. 212 (1), 27–44. https://doi.org/10.1016/j.chemgeo.2004.08.027.
- Kısakürek, B., James, R.H., Harris, N.B.W., 2005. Li and  $\delta^7$ Li in Himalayan rivers: proxies for silicate weathering? Earth Planet. Sci. Lett. 237 (3), 387–401. https://doi.org/10.1016/j.epsl.2005.07.019.
- Langmuir, D., 1997. Aqueous Environmental Geochemistry. Prentice Hall, NJ.

- Lemarchand, E., Chabaux, F., Vigier, N., Millot, R., Pierret, M.-C., 2010. Lithium isotope systematics in a forested granitic catchment (Strengbach, Vosges Mountains, France). Geochim. Cosmochim. Acta 74 (16), 4612–4628. https://doi.org/10.1016/j.gca.2010.04.057.
- Li, Q., Jew, A.D., Brown, G.E., Bargar, J.R., Maher, K., 2020. Reactive transport modeling of shale-fluid interactions after imbibition of fracturing fluids. Energy Fuels 34 (5), 5511–5523. https://doi.org/10.1021/acs.energyfuels.9b04542.
- Li, W., Liu, X.-M., 2020. Experimental investigation of lithium isotope fractionation during kaolinite adsorption: implications for chemical weathering. Geochim. Cosmochim. Acta 284, 156–172. https://doi.org/10.1016/j.gca.2020.06.025.
- Li, W., Liu, X.-M., Godfrey, L.V., 2018. Optimisation of lithium chromatography for isotopic analysis in geological reference materials by MC-ICP-MS. Geostand. Geoanal. Res. 43 (2), 261–276. https://doi.org/10.1111/ggr.12254.
- Liu, X.-M., Rudnick, R.L., McDonough, W.F., Cummings, M.L., 2013. Influence of chemical weathering on the composition of the continental crust: insights from Li and Nd isotopes in bauxite profiles developed on Columbia River Basalts. Geochim. Cosmochim. Acta 115, 73–91. https://doi.org/10.1016/j.gca.2013.03. 043.
- Maher, K., von Blanckenburg, F., 2016. Surface ages and weathering rates from <sup>10</sup>Be (meteoric) and <sup>10</sup>Be/<sup>9</sup>Be: insights from differential mass balance and reactive transport modeling. Chem. Geol. 446, 70–86. https://doi.org/10.1016/j.chemgeo. 2016.07.016.
- McLaughlin, R.J., Ellen, S., Blake Jr, M., Jayko, A.S., Irwin, W., Aalto, K., et al., 2000. Geology of the Cape Mendocino, Eureka, Garberville, and southwestern part of the Hayfork  $30\times60$  minute quadrangles and adjacent offshore area, northern California. In: U.S. Geological Survey Miscellaneous Field Studies Map MF-2336, vol. 1(100).
- Meybeck, M., 1987. Global chemical weathering of surficial rocks estimated from river dissolved loads. Am. J. Sci. 287 (5), 401–428. https://doi.org/10.2475/ajs. 287.5.401.
- Millot, R., Girard, J., 2007. Lithium isotope fractionation during adsorption onto mineral surfaces. In: Presented at the International Meeting on Clays in Natural & Engineered Barriers for Radioactive Waste Confinement. Lille, France.
- Millot, R., Guerrot, C., Vigier, N., 2004. Accurate and high-precision measurement of lithium isotopes in two reference materials by MC-ICP-MS. Geostand. Geoanal. Res. 28 (1), 153–159. https://doi.org/10.1111/jj.1751-908X.2004.tb01052.x.
- Millot, R., Vigier, N., Gaillardet, J., 2010. Behaviour of lithium and its isotopes during weathering in the Mackenzie Basin, Canada. Geochim. Cosmochim. Acta 74 (14), 3897–3912. https://doi.org/10.1016/j.gca.2010.04.025.
- Misra, S., Froelich, P.N., 2012. Lithium isotope history of Cenozoic Seawater: changes in silicate weathering and reverse weathering. Science 335 (6070), 818–823. https://doi.org/10.1126/science.1214697.
- Murphy, M.J., Porcelli, D., Pogge von Strandmann, P.A.E., Hirst, C.A., Kutscher, L., Katchinoff, J.A., et al., 2019. Tracing silicate weathering processes in the permafrost-dominated Lena River watershed using lithium isotopes. Geochim. Cosmochim. Acta 245, 154–171. https://doi.org/10.1016/j.gca.2018.10.024.
- Murphy, S.F., Brantley, S.L., Blum, A.E., White, A.F., Dong, H., 1998. Chemical weathering in a Tropical Watershed, Luquillo Mountains, Puerto Rico, II: rate and mechanism of biotite weathering. Geochim. Cosmochim. Acta 62 (2), 227–243. https://doi.org/10.1016/S0016-7037(97)00336-0.
- Palandri, J.L., Kharaka, Y.K., 2004. A Compilation of Rate Parameters of Water-Mineral Interaction Kinetics for Application to Geochemical Modeling. Geological Survey Menlo Park CA.
- Phan, T.T., Paukert Vankeuren, A.N., Hakala, J.A., 2018. Role of water-rock interaction in the geochemical evolution of Marcellus Shale produced waters. Int. J. Coal Geol. 191, 95–111. https://doi.org/10.1016/j.coal.2018.02.014.
- Pistiner, J.S., Henderson, G.M., 2003. Lithium-isotope fractionation during continental weathering processes. Earth Planet. Sci. Lett. 214 (1), 327–339. https://doi.org/10.1016/S0012-821X(03)00348-0.
- Pogge von Strandmann, P.A.E., Porcelli, D., James, R.H., van Calsteren, P., Schaefer, B., Cartwright, I., et al., 2014. Chemical weathering processes in the Great Artesian Basin: evidence from lithium and silicon isotopes. Earth Planet. Sci. Lett. 406, 24–36. https://doi.org/10.1016/j.epsl.2014.09.014.
- Pogge von Strandmann, P.A.E., Burton, K.W., Opfergelt, S., Eiríksdóttir, E.S., Murphy, M.J., Einarsson, A., Gislason, S.R., 2016. The effect of hydrothermal spring weathering processes and primary productivity on lithium isotopes: lake Myvatn, Iceland. Chem. Geol. 445, 4–13. https://doi.org/10.1016/j.chemgeo.2016.02.026.
- Pogge von Strandmann, P.A.E., Frings, P.J., Murphy, M.J., 2017. Lithium isotope behaviour during weathering in the Ganges Alluvial Plain. Geochim. Cosmochim. Acta 198, 17–31. https://doi.org/10.1016/j.gca.2016.11.017.
- Raymo, M.E., Ruddiman, W.F., Froelich, P.N., 1988. Influence of late Cenozoic mountain building on ocean geochemical cycles. Geology 16 (7), 649–653. https://doi.org/10.1130/0091-7613(1988)016<0649:IOLCMB>2.3.CO;2.
- Rempe, D.M., Dietrich, W.E., 2018. Direct observations of rock moisture, a hidden component of the hydrologic cycle. Proc. Natl. Acad. Sci. USA 115 (11), 2664–2669. https://doi.org/10.1073/pnas.1800141115.
- Riebe, C.S., Kirchner, J.W., Granger, D.E., Finkel, R.C., 2001. Strong tectonic and weak climatic control of long-term chemical weathering rates. Geology 29 (6), 511–514. https://doi.org/10.1130/0091-7613(2001)029<0511:STAWCC>2.0.CO;2.

- Rudnick, R.L., Tomascak, P.B., Njo, H.B., Gardner, L.R., 2004. Extreme lithium isotopic fractionation during continental weathering revealed in saprolites from South Carolina. Chem. Geol. 212 (1), 45–57. https://doi.org/10.1016/j.chemgeo.2004.08.
- Salve, R., Rempe, D.M., Dietrich, W.E., 2012. Rain, rock moisture dynamics, and the rapid response of perched groundwater in weathered, fractured argillite underlying a steep hillslope. Water Resour. Res. 48 (11). https://doi.org/10.1029/ 2012WR012583
- Sauzéat, L., Rudnick, R.L., Chauvel, C., Garçon, M., Tang, M., 2015. New perspectives on the Li isotopic composition of the upper continental crust and its weathering signature. Earth Planet. Sci. Lett. 428, 181–192. https://doi.org/10.1016/j. epsl.2015.07.032.
- Stallard, R.F., Edmond, J.M., 1983. Geochemistry of the Amazon, 2: the influence of geology and weathering environment on the dissolved load. J. Geophys. Res., Oceans 88 (C14), 9671–9688. https://doi.org/10.1029/JC088iC14p09671.
- Steefel, C.I., Appelo, C.A.J., Arora, B., Jacques, D., Kalbacher, T., Kolditz, O., et al., 2015. Reactive transport codes for subsurface environmental simulation. Comput. Geosci. 19 (3), 445–478. https://doi.org/10.1007/s10596-014-9443-x.
- Steinhoefel, G., Brantley, S.L., Fantle, M.S., 2021. Lithium isotopic fractionation during weathering and erosion of shale. Geochim. Cosmochim. Acta 295, 155–177. https://doi.org/10.1016/j.gca.2020.12.006.
- Tomascak, P.B., 2004. Developments in the understanding and application of lithium isotopes in the Earth and planetary sciences. Rev. Mineral. Geochem. 55 (1), 153–195. https://doi.org/10.2138/gsrmg.55.1.153.
- Torres, M.A., West, A.J., Clark, K.E., 2015. Geomorphic regime modulates hydrologic control of chemical weathering in the Andes-Amazon. Geochim. Cosmochim. Acta 166, 105–128. https://doi.org/10.1016/j.gca.2015.06.007.
- Tune, A.K., Druhan, J.L., Wang, J., Bennett, P.C., Rempe, D.M., 2020. Carbon dioxide production in bedrock beneath soils substantially contributes to forest carbon cycling. J. Geophys. Res., Biogeosci. 125 (12), e2020JG005795. https://doi.org/10. 1029/2020JG005795.
- Turkeltaub, T., Kurtzman, D., Bel, G., Dahan, O., 2015. Examination of groundwater recharge with a calibrated/validated flow model of the deep vadose zone. J. Hydrol. 522, 618–627. https://doi.org/10.1016/j.jhydrol.2015.01.026.
- Uhlig, D., von Blanckenburg, F., 2019. How slow rock weathering balances nutrient loss during fast forest floor turnover in Montane, temperate forest ecosystems. Front. Earth Sci. 7. https://doi.org/10.3389/feart.2019.00159.
- Wang, J.J., 2019. Linkages between fluid flow paths, reactive gases, and chemical weathering across a shale bedrock hillslope. Master's thesis. University of Illinois at Urbana-Champaign. http://hdl.handle.net/2142/105930.
- Wang, Q.-L., Chetelat, B., Zhao, Z.-Q., Ding, H., Li, S.-L., Wang, B.-L., et al., 2015. Behavior of lithium isotopes in the Changjiang River system: sources effects and response to weathering and erosion. Geochim. Cosmochim. Acta 151, 117–132. https://doi.org/10.1016/j.gca.2014.12.015.
- Wanner, C., Sonnenthal, E.L., Liu, X.-M., 2014. Seawater  $\delta^7$ Li: a direct proxy for global CO<sub>2</sub> consumption by continental silicate weathering? Chem. Geol. 381, 154–167. https://doi.org/10.1016/i.chemgeo.2014.05.005.
- Weynell, M., Wiechert, U., Schuessler, J.A., 2017. Lithium isotopes and implications on chemical weathering in the catchment of Lake Donggi Cona, northeastern Tibetan Plateau. Geochim. Cosmochim. Acta 213, 155–177. https://doi.org/10.1016/j.gca.2017.06.026.
- White, A.F., Bullen, T.D., Schulz, M.S., Blum, A.E., Huntington, T.G., Peters, N.E., 2001. Differential rates of feldspar weathering in granitic regoliths. Geochim. Cosmochim. Acta 65 (6), 847–869. https://doi.org/10.1016/S0016-7037(00)00577-9.
- White, A.F., Schulz, M.S., Stonestrom, D.A., Vivit, D.V., Fitzpatrick, J., Bullen, T.D., et al., 2009. Chemical weathering of a marine terrace chronosequence, Santa Cruz, California. Part II: solute profiles, gradients and the comparisons of contemporary and long-term weathering rates. Geochim. Cosmochim. Acta 73 (10), 2769–2803. https://doi.org/10.1016/j.gca.2009.01.029.
- Williams, L.B., Hervig, R.L., 2005. Lithium and boron isotopes in illite-smectite: the importance of crystal size. Geochim. Cosmochim. Acta 69 (24), 5705–5716. https://doi.org/10.1016/j.gca.2005.08.005.
- Wimpenny, J., Gíslason, S.R., James, R.H., Gannoun, A., Pogge Von Strandmann, P.A.E., Burton, K.W., 2010. The behaviour of Li and Mg isotopes during primary phase dissolution and secondary mineral formation in basalt. Geochim. Cosmochim. Acta 74 (18), 5259–5279. https://doi.org/10.1016/j.gca.2010.06.028.
- Wolery, T.J., Jackson, K.J., Bourcier, W.L., Bruton, C.J., Viani, B.E., Knauss, K.G., Delany, J.M., 1990. Current status of the EQ3/6 software package for geochemical modeling. In: Chemical Modeling of Aqueous Systems II, vol. 416. American Chemical Society, pp. 104–116.
- Zhang, J.-W., Zhao, Z.-Q., Yan, Y.-N., Cui, L.-F., Wang, Q.-L., Meng, J.-L., Li, X.-D., Liu, C.-Q., 2021a. Lithium and its isotopes behavior during incipient weathering of granite in the eastern Tibetan Plateau, China. Chem. Geol. 559, 119969. https://doi.org/10.1016/j.chemgeo.2020.119969.
- Zhang, X., Saldi, G.D., Schott, J., Bouchez, J., Kuessner, M., Montouillout, V., Henehan, M., Gaillardet, J., 2021b. Experimental constraints on Li isotope fractionation during the interaction between kaolinite and seawater. Geochim. Cosmochim. Acta 292, 333–347. https://doi.org/10.1016/j.gca.2020.09.029.